



Antenna-enhanced high harmonic generation in a wide-bandgap semiconductor ZnO

KOTARO IMASAKA, TOMOHIRO KAJI, TSUTOMU SHIMURA, AND SATOSHI ASHIHARA*

Institute of Industrial Science, The University of Tokyo, 4-6-1 Komaba, Meguro-ku, Tokyo 1538505, Japan

*ashihara@iis.u-tokyo.ac.jp

Abstract: High harmonic generation (HHG) in solids has great potential for coherent extreme ultraviolet (EUV) sources, all-optical band-structure reconstruction, and electron dynamics metrology. Solid HHG driven by plasmonic near-fields will open a new paradigm, enabling high repetition-rate HHG with a compact laser, HHG manipulation with meta-surfaces, and precise control over carrier trajectory. In this paper, we demonstrate antenna-enhanced HHG in a wide-bandgap semiconductor ZnO. By exploiting gold nano-antennas resonating at the driver wavelength of 2 μm , we successfully trigger HHG at input intensity of $\sim 0.02 \text{ TW/cm}^2$ and observe harmonic radiations up to 9th-order. Orders-of-magnitude enhanced conversion efficiency at the hot-spots brings about ten-fold enhancement in the total yield. The spectral selection rule is found to reflect crystal symmetry, suggesting the possibility of nano-scaled EUV sources and band-structure reconstruction.

© 2018 Optical Society of America under the terms of the [OSA Open Access Publishing Agreement](#)

1. Introduction

High harmonic generation (HHG) in gaseous media [1–3] has proved useful for generating coherent attosecond radiation in extreme ultraviolet (EUV) and soft X-ray regions [4], imaging molecular orbitals [5, 6], etc., and opened an innovative research area of attosecond physics [7, 8]. HHG under the non-perturbative regime has been observed in a solid (ZnO) as well in 2011 [9], since when solid HHG has been attracting growing attention [10–15]. In analogy to the three-step model for gaseous HHG [2], the mechanism of solid HHG is described as inter-band tunneling of an electron, acceleration of a crystal electron/hole, and the following high harmonic (HH) radiation via intra-band current and/or inter-band polarization [15, 16]. Because of high atomic density, crystal symmetry, and characteristic band structure, solid HHG is expected to have great potential for efficient and sophisticated EUV light-sources [10, 12, 13, 17], all-optical band-structure reconstruction [11, 18], probing electron dynamics [11, 19], and to develop condensed-phase attosecond physics.

Few-cycle pulses in the mid-infrared (MIR) range are suited for driving strong-field phenomena in solids, because low-frequency drivers tend to excite electrons in the tunneling regime, provide efficient ponderomotive acceleration, and are able to apply intense electric field without materials damage [20]. Generation of energetic MIR pulses, however, usually requires an optical parametric amplifier based on a high-power chirped-pulse amplifier.

A smart way to induce strong-field phenomena with moderate driver-laser power is to confine ultrashort optical field by using nano-antennas or other nano-structures. So far, metal antennas resonating at MIR frequencies [21, 22] have been used for the strong-field photoemission [23] and for the nonlinear vibrational spectroscopy [24, 25]. Very recently, pioneering works on solid HHG utilizing nano-structures have been reported [26–28]. Han et al. [26] used a metal-coated sapphire nano-cone to produce HH radiations in EUV range. Sivis et al. [27] used nano-structured and ion-implanted semiconductors to enhance HHG and to manipulate its spatial distribution. Vampa et al. [28] used metallic antennas to assist HHG from silicon with small bandgap (E_g) of $\sim 1.2 \text{ eV}$. In these pioneering works, only odd-order harmonics were observed.

In this paper, we demonstrate antenna-enhanced HHG in a wide-bandgap semiconductor ZnO ($E_g \sim 3.3$ eV) into the deep ultraviolet (DUV) range. By exploiting Au antennas resonating at the MIR driver wavelength of $2\text{ }\mu\text{m}$, the non-perturbative HHG is induced at the substantially reduced input intensity, and harmonic radiations up to 9th-order is observed. In the presence of the antennas, orders-of-magnitude enhanced conversion efficiency at the hot-spots brings about ten-fold enhancement in the total harmonic yield, in spite of their limited volume. Only odd-order harmonics are generated when the antennas oriented along a symmetry-preserved crystal axis are excited, whereas both odd- and even-order harmonics are generated when the antennas oriented along the symmetry-broken crystal axis are excited. The finding that the spectral selection rule reflects the crystal symmetry suggests the possibility of nano-scaled EUV sources and band-structure reconstruction of nano-materials. Successful demonstration of antenna-enhanced HHG indicates that plasmonic near-fields are useful for manipulating HHG with meta-surfaces and driving a variety of strong-field phenomena in wide-gap semiconductors.

2. Devices and methods

For the purpose of enhanced HHG in ZnO, we design a 2D array of a rod-shaped Au nano-antenna. We fabricate it on a 0.5-mm-thick *a*-cut ZnO crystal (MTI Corp.) by the electron-beam lithography and the lift-off process, where evaporation of Au is followed by that of 5-nm-thick Cr adhesion layer. The scanning electron microscope (SEM) image is shown in Fig. 1(a). Each antenna has the dimensions of 570 nm in length, 310 nm in width, and 100 nm in thickness. We adapt this thick shape to increase the damage resistance as well as the hot-spot volume. The array period along the shorter (longer) axis of an individual antenna is set to be 900 nm (700 nm) to increase the near-field enhancement through the nearly collective resonance [24] (to increase the hot-spot density while avoiding near-field couplings between antennas). Each antenna is oriented parallel to either *m*-axis (sample I) or *c*-axis (sample II). The extinction spectrum of the antenna array, measured by the Fourier-transform infrared spectroscopy at normal incidence, is shown in Fig. 1(b), together with an extinction curve calculated by the finite-difference time-domain (FDTD) method. The broader linewidth for the measured spectrum may be due to inhomogeneous distribution of antenna size/shape. A near-field distribution inside the ZnO substrate (2-nm beneath the air-ZnO interface, normalized with an incident field) calculated for a wavelength of $2\text{ }\mu\text{m}$ is shown in Fig. 1(c). The intensity enhancement factor in the vicinity of the antenna end (2-nm beneath the air-ZnO interface) is ~ 80 at $2\text{ }\mu\text{m}$, as displayed in the upper panel of Fig. 1(b).

A schematic of our experimental setup is shown in Fig. 1(d). A driver source is a MIR pulse (center wavelength of $2\text{ }\mu\text{m}$, temporal duration of 100 fs), generated from an optical parametric amplifier (OPA, 2-mm-thick β -BaB₂O₄, type II) pumped by a Ti: sapphire regenerative amplifier (1 kHz, 1 mJ). The samples are exposed at normal incidence by linearly-polarized MIR pulses with a beam diameter of $270\text{ }\mu\text{m}$. The driver pulse is incident on a bare surface of a substrate and exposes the antennas from the substrate-side. The HH spectra are measured with a diffraction grating (2400 or 1800 lines/mm) and a photomultiplier tube (PMT, H10722-113, Hamamatsu Photonics). The Rochon prism is used for the polarization-resolved detection. Here we calibrate the spectral energy (J/THz) by considering the radiant sensitivity and the electron multiplication factor of PMT, the transmittances of the lens and the prism, and the diffraction efficiency of the grating. Because the resonant bandwidth of the antenna is much broader than the pulse spectrum (a black line in Fig. 1(b)), enhanced near-field is expected to have identical waveform to the incident one except for a phase retardation of $\pi/2$ [22, 24].

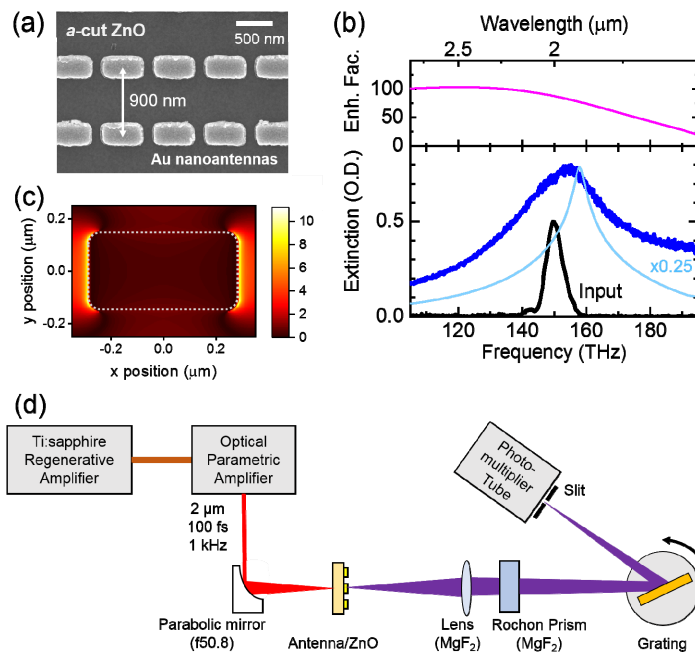


Fig. 1. (a) A SEM image of an antenna array fabricated on ZnO. (b) The measured extinction spectrum (blue) is shown with the calculated extinction spectrum (light blue) and the calculated intensity enhancement factor (pink). A black line represents the input pulse spectrum. (c) A simulated near-field distribution inside the ZnO substrate (2-nm beneath the air-ZnO interface). The dotted line shows the antenna area. (d) A schematic of the experimental setup.

3. Results and discussions

We re-investigate the input-polarization dependence of the HH spectrum for the bare bulk ZnO crystal [9, 12]. Figure 2 shows the HH spectral energy (J/THz) measured for an *a*-cut bulk ZnO crystal of 0.5 mm thickness without antennas, at varied angle θ between the input polarization E_{in} and the crystallographic *c*-axis. Here the input peak intensity is set to be 0.29 TW/cm² (an electric field of 1.5 V/nm) and the HH spectrum is plotted for the dominating polarization component which is parallel to the input one. Only odd-order harmonics (H5, H7, and H9) are observed at $\theta = 90^\circ$ and both odd- and even-order harmonics (H5–H9) are observed at $\theta = 0^\circ$. This behavior agrees with earlier studies [9, 12] and reflects the breaking of inversion-symmetry along *c*-axis.

Figure 3 shows the HH spectrum of the ZnO sample with and without antennas for each of (a) the sample I and (b) the sample II, measured at the input intensity of 0.10 TW/cm² (the electric field of 0.87 V/nm and the pulse energy of 2.8 μJ). Here the linear polarization of the input pulse is set parallel to the longer axes of the antennas, and therefore to *m*-axis for the sample I and to *c*-axis for the sample II. The HH spectra shown in Figs. 3(a) and 3(b) are for the dominating polarization components which are parallel to the input polarization.

For the sample I with antennas, odd-order harmonics (H5, H7, and H9) extending to the 9th-order (222 nm) and a band centered at 380 nm, attributed to the bandgap fluorescence (FL), are observed. For the sample II with antennas, both odd- and even-order harmonics (H5–H9), together with FL, are observed. In this way, the spectral selection rule, being consistent with the polarization-angle dependence shown in Fig. 2, is found to reflect precisely the crystal symmetry of the substrate ZnO. This fact indicates that harmonic radiations originate from the dielectric substrate (not from the metal antennas) and that the near-field parallel to the longer-axis of each antenna contributes dominantly to the harmonic

signals (see Appendix C for details). From Fig. 3(a) for the sample I, one finds that H5 and H7 are enhanced, and H9 and FL are newly generated, because of the antennas. Similarly, one finds in Fig. 3(b) for the sample II that H5, H6, and H7 are enhanced, and H8, H9 and FL are newly generated because of the antennas. Figure 3(c) displays the HH spectra for the sample II, measured at lower intensity of 0.047 TW/cm^2 (an electric field of 0.59 V/nm). It is found that remarkable enhancement in the HH yield is observed also for H5 and H7 at this lower excitation. Quantitatively speaking, ten-fold enhancement in the total yield is observed for H5 and H7 at the input intensity of 0.047 TW/cm^2 (see Fig. 3 (c)) and for H8 and H9 at 0.10 TW/cm^2 (see Fig. 3(b)).

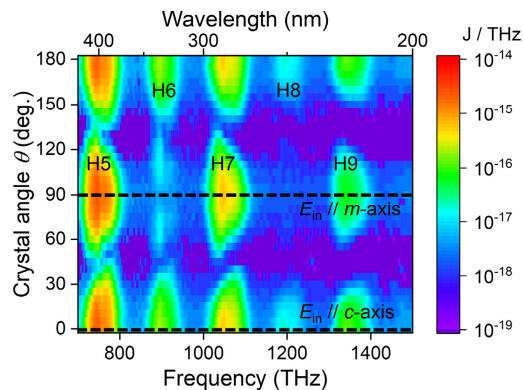


Fig. 2. Polarization-angle dependence of the HH spectrum measured for an *a*-cut bare ZnO crystal (without antennas), measured at input intensity of 0.29 TW/cm^2 (an electric field of 1.5 V/nm). The HH spectrum is plotted for a polarization component parallel to the input polarization.

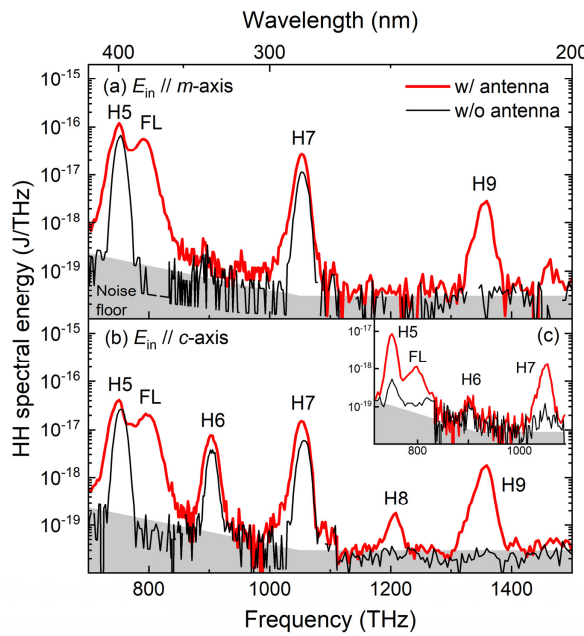


Fig. 3. The HH spectrum measured at input intensity of 0.10 TW/cm^2 (an electric field of 0.87 V/nm) (a) for the sample I ($E_{\text{in}} \parallel m\text{-axis}$) and (b) for the sample II ($E_{\text{in}} \parallel c\text{-axis}$). The red (black) lines indicate the HH spectra generated from ZnO with (without) antennas. (c) The HH spectra for the sample II, measured at input intensity of 0.047 TW/cm^2 (an electric field of 0.59 V/nm).

Figure 4 displays the input-intensity dependence of the HH spectral energy for each harmonics (H5–H9) and for the fluorescence (FL), measured for the sample II with/without antennas. Here again, the input polarization is set parallel to the antenna longer-axis and therefore to c -axis, and the HH spectrum is measured for the polarization parallel to the input one. One can see that the onset of HHG shifts to lower intensity due to the antennas, and that enhancement of HHG is more remarkable at weaker excitation. Note that the Au antennas are not physically damaged at the measured intensity range of less than 0.1 TW/cm^2 , but are damaged at intensity well exceeding this value.

In Fig. 4, the dependence for each harmonic order (H5–H9) and FL are displayed with a line expressing the multi-photon dependence. Each of the bulk HHGs follows the multi-photon law at lower intensity but deviates from it at higher intensity. Such kink in the slope indicates the transition from the perturbative to the non-perturbative regime [9, 12]. Regarding H7, the slope for the antenna-enhanced case is smaller than 7 even at $\sim 0.02 \text{ TW/cm}^2$. This fact indicates that the plasmonic near-field is strong enough to induce the non-perturbative HHG at such low illumination. The intensity enhancement of ~ 80 (see Fig. 1(b)) suggests that the local intensity may reach $\sim 1.6 \text{ TW/cm}^2$. As the input intensity increases further, however, HH radiation from the bulk grows to compete with that from the plasmonic hot-spots. This is because the plasmonic hot-spots have only limited volume and because HHG at the hot-spots tend to display less steep intensity dependence (than the multi-photon law), characteristic to the strong-field regime. These trends generally hold for the other orders, too (an exception is H6). The FL yield for the antenna-enhanced sample exhibits a slope of ~ 3.7 , which is smaller than the multi-photon dependence of 5.3 for the bandgap transition. The FL is not observed from the bare bulk sample at the measured intensity range of $< 0.5 \text{ TW/cm}^2$.

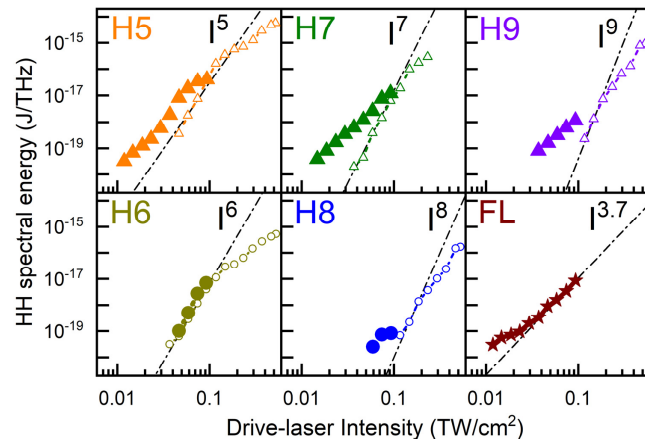


Fig. 4. The input-intensity dependence of the HH spectral energy, measured for the sample II ($E_{\text{in}} // c$ -axis) with (filled markers) and without (open markers) antennas: each panel shows the dependence for each of H5–H9 and FL with a line expressing the multi-photon law.

From the measured HH spectra, we estimate the conversion efficiency for the plasmonic near-fields (or the hot-spots), η_{nano} , and that for the bulk, η_{bulk} . By considering the effective volume for each, we calculate the conversion efficiency per unit volume (or “the local conversion efficiency”), $\eta_{\text{nano},V}$ and $\eta_{\text{bulk},V}$, to obtain the ratio $\eta_{\text{nano},V}/\eta_{\text{bulk},V}$ (see Appendix D for details). For H7 at the input intensity of 0.037 TW/cm^2 , we estimate $\eta_{\text{nano}} = 1.5 \times 10^{-11}$ and $\eta_{\text{bulk}} = 7.0 \times 10^{-13}$ to obtain $\eta_{\text{nano}}/\eta_{\text{bulk}} = 21$ and $\eta_{\text{nano},V}/\eta_{\text{bulk},V} = 1.2 \times 10^3$. For H9, at the same input intensity, we estimate $\eta_{\text{nano}} = 1.5 \times 10^{-12}$ and $\eta_{\text{bulk}} = 2.7 \times 10^{-16}$ (estimated by

extrapolation) to obtain $\eta_{\text{nano}} / \eta_{\text{bulk}} = 5.6 \times 10^3$ and $\eta_{\text{nano,V}} / \eta_{\text{bulk,V}} = 2.3 \times 10^5$. Here we conclude that the total yield is increased by a factor of 10^1 – 10^3 and the local conversion efficiency is increased by a factor of 10^3 – 10^5 , due to the plasmonic near-field enhancement.

As shown in Figs. 3(a), 3(b) and 4, FL is newly generated by the presence of antennas. It is naturally expected that carrier excitation via Zener tunneling is accelerated by the near-field enhancements. But the observed substantial enhancement by the presence of antennas implies additional mechanisms. Because the fundamental resonance of the antenna is far from the bandgap transition, acceleration of the interband absorption/emission rate due to the coupling to the antenna mode seems unlikely [29]. Rather than that, carrier transfer from Au to ZnO via the optical-field-induced tunneling [30, 31] and carrier multiplication by the impact ionization [32] seem plausible. Further study is necessary to clarify the mechanisms in detail.

Before summarizing, it would be useful to discuss the emission properties of the antenna-enhanced solid HHG, by comparing them with the properties of the conventional lower-order harmonic generation from metal nanoparticles. So far, plasmonic near-field enhancement has been used for second-harmonic generation (SHG) from metal nanoparticles [33] and third-harmonic generation (THG) from metal-dielectric hybrid nanostructures [34, 35]. Harmonic radiation originates from metal surface in the former case and from both metal surface and adjacent dielectric media in the latter case [34, 35]. In our antenna-enhanced solid HHG, in contrast, harmonic radiations originate dominantly from the dielectric substrate, as indicated by the result that the spectral selection rule precisely reflects the crystal symmetry of the substrate ZnO. This fact suggests the possibility of controlling temporal, spectral, and vectorial properties of HHG with crystal symmetry under plasmonic enhancement, and that of band-structure reconstruction at nano-scale.

It is known that SHG from metal surface is suppressed if the metal particle has a geometrical shape of inversion symmetry. This is because the sign of the second-order susceptibility (and also the sign of any other even-order susceptibility) varies according to the surface normal, and because harmonic radiations from different positions on metal surface interfere destructively with each other in the far-field. In the antenna-enhanced solid HHG, in contrast, HH radiations from different positions inside the major hot-spots (see Appendix C for details) interfere constructively with each other in the far-field, regardless of the harmonic order. This is because the microscopic structure, from which any nonlinearity originates, is homogeneous within the crystalline ZnO substrate.

4. Conclusions

In conclusion, we demonstrate antenna-enhanced HHG in a wide-bandgap semiconductor ZnO and observe up to H9 in DUV range. By exploiting the gold antennas, the non-perturbative HHG is induced at substantially reduced intensity of ~ 0.02 TW/cm². In the presence of the antennas, orders-of-magnitude enhanced conversion efficiency at the hot-spots brings about ten-fold enhancement in the total harmonic yield. We observe not only odd-order harmonics but also even-order harmonics, depending on the orientation of the antennas (and therefore the direction of the near-fields) with respect to the symmetry-broken crystal axis. The fact that the spectral selection rule precisely reflects the crystal symmetry indicates that harmonic radiations originate from dielectric substrate and suggests the possibility of nano-scale EUV sources, sophisticated control over HH waveforms, and band-structure reconstruction of nano-materials. The successful demonstration of antenna-enhanced HHG indicates that the plasmonic near-fields are useful for manipulating HHG with metasurfaces and for driving a variety of strong-field phenomena in wide-gap semiconductors, and will pave the way to nano-scale light-wave electronics.

Appendix A: a nano-antenna model

Near-field distribution around an arrayed resonant nano-antenna is numerically simulated by the finite-difference time-domain method (Lumerical, ver. 8). The model mimics the sample

used in our experiments, namely, an arrayed Au antenna on an *a*-cut ZnO single crystal. As described in the main part, each antenna has the dimensions of 570 nm in length (we term this dimension as *x*-axis), 310 nm in width (*y*-axis), and 100 nm in thickness (*z*-axis), and the array period along *x*-axis (*y*-axis) is 700 nm (900 nm). In the simulations, the antenna array is illuminated by an ultrashort optical pulse which contains the wavelength component of 2 μm, propagates along *z*-axis, and is linearly polarized along *x*-axis.

Temporal waveform of electric-field is calculated at each position in the presence of the antenna and is Fourier-transformed into the (complex) spectral amplitude $E_{x,y,z}^{\text{near}}(\omega)$ for a frequency ω and for each of *x*, *y*, and *z* components. The spectral amplitude of the incident electric-field $E^{\text{inc}}(\omega)$ is obtained from the same calculation but in the absence of the antenna. Then the spectral transfer function $H(\omega)$ is defined at each position as $H_{x,y,z}(\omega) = E_{x,y,z}^{\text{near}}(\omega) / E^{\text{inc}}(\omega)$, where we term $|H_{x,y,z}(\omega)|$ as the magnitude of the field enhancement.

Appendix B: the hot-spot volume

Figure 5 displays the magnitude of the field enhancement for the *x*-component at the wavelength of 2 μm, (a) at a plane of *z* = -2 nm (away from the air-ZnO interface by 2 nm into ZnO) and (b) at a plane of *y* = 0, which intersects with the antenna at its center. Note that Fig. 5(a) is identical to Fig. 1(c). From the simulated near-field distribution, we estimate the spatial extent of the hot-spot in each direction, as the intensity integrated with respect to distance divided by the intensity at the immediate vicinity of the antenna end. By using the estimated spatial extents, we calculate the hot-spot volume inside ZnO as 35 nm (*x*) × 262 nm (*y*) × 24 nm (*z*) = 2.2×10^5 nm³ for a single hot-spot and, correspondingly, 4.3×10^5 nm³ per an antenna.

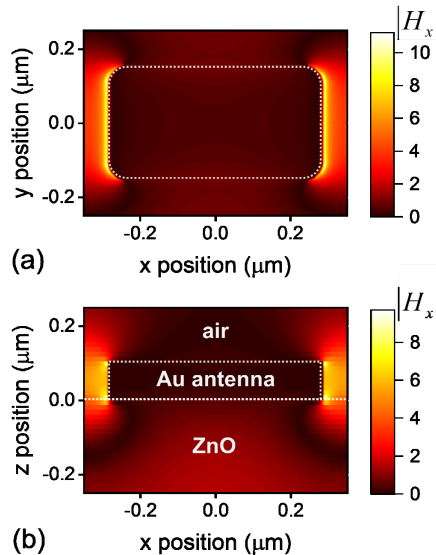


Fig. 5. The magnitude of the field enhancement for the *x*-component at the wavelength of 2 μm (a) at a plane of *z* = -2 nm (inside ZnO) and (b) at a plane of *y* = 0 which intersects with the antenna at its center.

Appendix C: contribution of perpendicular components.

Figures 6(a)–6(c) display the imaginary part of the transfer function for each of the *x*, *y*, and *z*-components, $\text{Im}[H_{x,y,z}(\omega)]$, at the arrayed-antenna resonance and at a plane of *z* = -2 nm

(away from the air-ZnO interface by 2 nm into ZnO). Here we note that the imaginary part is maximized at the antenna resonance frequency. The spatial distribution of each component is reasonably understood from the nature of an oscillating electric dipole.

By comparing $\text{Im}[H_x(\omega)]$ and $\text{Im}[H_y(\omega)]$, we find that the former has larger absolute value. We also find that the sign (and therefore the phase) of the x -component, $\text{Im}[H_x(\omega)]$, is the same for two of the hot-spots at the antenna ends. It indicates that harmonic radiations driven by the x -component of the electric-field at two of the hot-spots ($x \sim \pm 285$ nm) interfere constructively with each other at large distance in z -direction. In contrast, the sign (and therefore the phase) of the y -component, $\text{Im}[H_y(\omega)]$, is different between any of the two adjacent hot-spots among four of the hot-spots ($y \sim \pm 155$ nm). It indicates that harmonic radiations driven by the y -component of the electric-field at different hot-spots interfere destructively with each other at large distance in z -direction. Furthermore, harmonic radiations driven by the y -component should be mostly polarized along y -axis, which we confirm from the polarization-resolved measurement on harmonic radiations from the bulk sample. Therefore the y -component of the near-field, $\text{Im}[H_y(\omega)]$, should have only minor contribution to the measured “ x -polarized” high-harmonic signals than the x -component, $\text{Im}[H_x(\omega)]$.

The z -component, $\text{Im}[H_z(\omega)]$, has an absolute value which is comparable to that of $\text{Im}[H_x(\omega)]$, but should have much smaller contribution to the measured signals because of the following reasons. First, the hot-spots for the z -component exist mostly under the antenna and the harmonics generated in the area cannot reach our detector. Second, harmonics driven by the z -component of the electric-field should be polarized along z -axis, and therefore will not propagate into z -direction.

In this way, the simulated near-field distributions suggest that the near-field component which is parallel to the longer axis of the antenna dominantly contributes to the measured “ x -polarized” high-harmonic signals. This hypothesis is, in fact, supported by the following two experiments. When the longer axis of the antenna (and the input polarization) is oriented along m -axis on an a -cut substrate, even-order harmonics are not observed as shown in Fig. 3(a), although y -component is in parallel to the symmetry-breaking c -axis. In the additional experiment where the longer-axis of the antenna (and the input polarization) is oriented along m -axis on a c -cut substrate, even-order harmonics are not observed (results not shown), although z -component is in parallel to the symmetry-breaking c -axis.

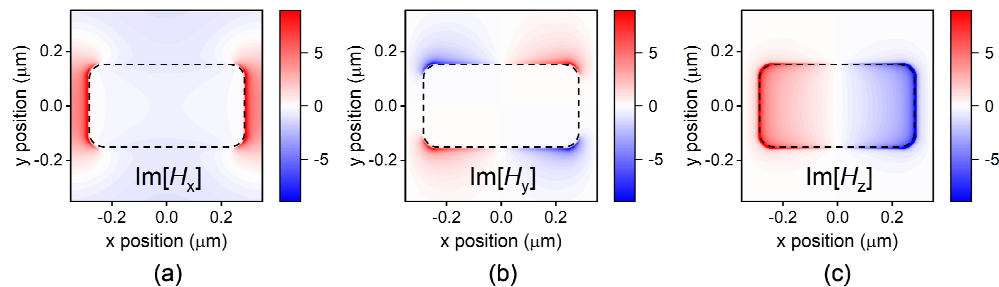


Fig. 6. The imaginary part of the transfer function for each of the (a) x , (b) y , and (c) z -components, $\text{Im}[H_{x,y,z}(\omega)]$, at a plane of $z = -2$ nm (away from the air-ZnO interface by 2 nm into ZnO). The dashed line indicates the area covered by the gold antenna.

Appendix D: Conversion efficiency

We calculate the output pulse energy for each harmonics by integrating the measured spectral density (unit of J/THz) for the relevant spectral range. Here we define the output pulse energy of a certain harmonics as $S_{w/}$ and $S_{w/o}$, for the sample with and without antennas, respectively. For the bare bulk sample, the output energy is expressed as

$$S_{w/o} = S'_{\text{bulk}} \times T_{\text{air/ZnO}} \quad (1)$$

where S'_{bulk} denotes the harmonic energy inside the bulk crystal and $T_{\text{air/ZnO}}$ denotes the energy transmittance at the output air-ZnO interface. Here we calculate $T_{\text{air/ZnO}}$ from the reflectance data in a literature [36]. For the sample with antennas, the output energy is expressed as

$$S_{w/} = S'_{\text{nano}} \times T_{\text{air/ZnO}} + S'_{\text{bulk}} \times T_{\text{air/Au/ZnO}} \quad (2)$$

where S'_{nano} denotes the harmonic energy inside the hot-spots and $T_{\text{air/Au/ZnO}}$ denotes the energy transmittance at the output air-ZnO interface covered with Au-antennas. Here we assume, for simplicity, that the total harmonic energy is an incoherent summation of the harmonic energy from the bulk and that from the hot-spots. We find from the transmission measurements that the ratio of $T_{\text{air/Au/ZnO}}$ to $T_{\text{air/ZnO}}$ is almost constant (~ 0.5) in the wavelength range of 400–800 nm. Here we assume that this ratio holds further down to the wavelengths of H7–H9. The internal conversion efficiency is calculated as $\eta_{\text{nano}} = S'_{\text{nano}} / S_{\text{in}}$ and $\eta_{\text{bulk}} = S'_{\text{bulk}} / S_{\text{in}}$, for the plasmonic hot-spots and for the bulk, respectively, where S_{in} is the input pulse energy. Then we obtain the conversion efficiency per unit volume (or the local conversion efficiency), $\eta_{\text{nano,V}}$ and $\eta_{\text{bulk,V}}$, by considering the hot-spot volume per antenna of $4.3 \times 10^5 \text{ nm}^3$ (see section “the hot-spot volume”), and the corresponding bulk volume of $700 \text{ nm} \times 900 \text{ nm} \times L_{\text{abs}}$ (L_{abs} denotes the penetration depth: 40 nm for H7 and 28 nm for H9 [36]).

In the following, we estimate the conversion efficiencies of H7 and H9 at the input intensity of 0.037 TW/cm^2 (an electric-field of 0.53 V/nm, the pulse energy of $1.0 \times 10^{-6} \text{ J}$).

For H7, from the measured values of $S_{w/o} = 6.4 \times 10^{-19} \text{ J}$ and $S_{w/} = 1.4 \times 10^{-17} \text{ J}$ (the corresponding spectral energies appear in Fig. 4), we obtain the internal harmonic energies of $S'_{\text{bulk}} = 7.3 \times 10^{-19} \text{ J}$ and $S'_{\text{nano}} = 1.5 \times 10^{-17} \text{ J}$. Then we estimate the conversion efficiencies as $\eta_{\text{nano}} = 1.5 \times 10^{-11}$ and $\eta_{\text{bulk}} = 7.0 \times 10^{-13}$, to obtain $\eta_{\text{nano}} / \eta_{\text{bulk}} = 21$. By considering the effective volumes, we obtain the enhancement factor of the local conversion efficiency as $\eta_{\text{nano,V}} / \eta_{\text{bulk,V}} = 1.2 \times 10^3$.

For H9, from the measured value of $S_{w/} = 1.4 \times 10^{-18} \text{ J}$ (the corresponding spectral energy appears in Fig. 4) and $S_{w/o} = 2.5 \times 10^{-22} \text{ J}$ (obtained by extrapolation assuming the multi-photon law shown in Fig. 4), we obtain $S'_{\text{bulk}} = 2.8 \times 10^{-22} \text{ J}$ and $S'_{\text{nano}} = 1.6 \times 10^{-18} \text{ J}$. Then we estimate $\eta_{\text{nano}} = 1.5 \times 10^{-12}$ and $\eta_{\text{bulk}} = 2.7 \times 10^{-16}$ to obtain $\eta_{\text{nano}} / \eta_{\text{bulk}} = 5.6 \times 10^3$ and $\eta_{\text{nano,V}} / \eta_{\text{bulk,V}} = 2.3 \times 10^5$.

Funding

Japan Society for the Promotion of Science (JSPS) (MEXT KAKENHI 16K13694, 18K19030, Bilateral Joint Research Projects 1007490).

Acknowledgment

The samples were fabricated at VLSI Design and Education Center (VDEC), the University of Tokyo. We thank Prof. K. Hirakawa (Institute of Industrial Science, the University of Tokyo) for technical supports in the fabrication/observation of metal nanostructures.

References

1. M. Ferray, A. L'Huillier, X. F. Li, L. A. Lomprk, G. Mainfray, and C. Manus, "Multiple-harmonic conversion of 1064 nm radiation in rare gases," *J. Phys. At. Mol. Opt. Phys.* **21**(3), L31–L35 (1988).
2. P. B. Corkum, "Plasma perspective on strong field multiphoton ionization," *Phys. Rev. Lett.* **71**(13), 1994–1997 (1993).
3. T. Brabec and F. Krausz, "Intense few-cycle laser fields: Frontiers of nonlinear optics," *Rev. Mod. Phys.* **72**(2), 545–591 (2000).
4. J. Li, X. Ren, Y. Yin, K. Zhao, A. Chew, Y. Cheng, E. Cunningham, Y. Wang, S. Hu, Y. Wu, M. Chini, and Z. Chang, "53-attosecond X-ray pulses reach the carbon K-edge," *Nat. Commun.* **8**(1), 186 (2017).
5. J. Itatani, J. Levesque, D. Zeidler, H. Niikura, H. Pépin, J. C. Kieffer, P. B. Corkum, and D. M. Villeneuve, "Tomographic imaging of molecular orbitals," *Nature* **432**(7019), 867–871 (2004).
6. O. Smirnova, Y. Mairesse, S. Patchkovskii, N. Dudovich, D. Villeneuve, P. Corkum, and M. Y. Ivanov, "High harmonic interferometry of multi-electron dynamics in molecules," *Nature* **460**(7258), 972–977 (2009).
7. P. B. Corkum and F. Krausz, "Attosecond science," *Nat. Phys.* **3**(6), 381–387 (2007).
8. F. Krausz and M. Ivanov, "Attosecond physics," *Rev. Mod. Phys.* **81**(1), 163–234 (2009).
9. S. Ghimire, A. D. DiChiara, E. Sistrunk, P. Agostini, L. F. DiMauro, and A. Reis, "Observation of high-order harmonic generation in a bulk crystal," *Nat. Phys.* **7**(2), 138–141 (2011).
10. O. Schubert, M. Hohenleutner, F. Langer, B. Urbanek, C. Lange, U. Huttner, D. Golde, T. Meier, M. Kira, S. W. Koch, and R. Huber, "Sub-cycle control of terahertz high-harmonic generation by dynamical Bloch oscillations," *Nat. Photonics* **8**(2), 119–123 (2014).
11. T. T. Luu, M. Garg, S. Y. Kruchinin, A. Moulet, M. T. Hassan, and E. Goulielmakis, "Extreme ultraviolet high-harmonic spectroscopy of solids," *Nature* **521**(7553), 498–502 (2015).
12. S. Gholam-Mirzaei, J. Beetar, and M. Chini, "High harmonic generation in ZnO with a high-power mid-IR OPA," *Appl. Phys. Lett.* **110**(6), 061101 (2017).
13. Y. S. You, D. A. Reis, and S. Ghimire, "Anisotropic high-harmonic generation in bulk crystals," *Nat. Phys.* **13**(4), 345–349 (2017).
14. N. Yoshikawa, T. Tamaya, and K. Tanaka, "High-harmonic generation in graphene enhanced by elliptically polarized light excitation," *Science* **356**(6339), 736–738 (2017).
15. H. Liu, Y. Li, Y. S. You, S. Ghimire, T. F. Feinz, and D. A. Reis, "High-harmonic generation from an atomically thin semiconductor," *Nat. Phys.* **13**(3), 262–265 (2016).
16. G. Vampa, T. J. Hammond, N. Thiré, B. E. Schmidt, F. Légaré, C. R. McDonald, T. Brabec, and P. B. Corkum, "Linking high harmonics from gases and solids," *Nature* **522**(7557), 462–464 (2015).
17. F. Langer, M. Hohenleutner, U. Huttner, S. W. Koch, M. Kira, and R. Huber, "Symmetry-controlled temporal structure of high-harmonic carrier fields from a bulk crystal," *Nat. Photonics* **11**(4), 227–231 (2017).
18. G. Vampa, T. J. Hammond, N. Thiré, B. E. Schmidt, F. Légaré, C. R. McDonald, T. Brabec, D. D. Klug, and P. B. Corkum, "All-Optical Reconstruction of Crystal Band Structure," *Phys. Rev. Lett.* **115**(19), 193603 (2015).
19. M. Garg, M. Zhan, T. T. Luu, H. Lakhotia, T. Klostermann, A. Guggenmos, and E. Goulielmakis, "Multi-petahertz electronic metrology," *Nature* **538**(7625), 359–363 (2016).
20. C. Vozzi, M. Negro, and S. Stagira, "Strong-field phenomena driven by mid-infrared ultrafast sources," *J. Mod. Opt.* **59**(15), 1283–1302 (2012).
21. K. B. Crozier, A. Sundaramurthy, G. S. Kino, and C. F. Quate, "Optical antennas: Resonators for local field enhancement," *J. Appl. Phys.* **94**(7), 4632–4642 (2003).
22. F. Kusa and S. Ashihara, "Spectral response of localized surface plasmon in resonance with mid-infrared light," *J. Appl. Phys.* **116**(15), 153103 (2014).
23. F. Kusa, K. E. Echternkamp, G. Herink, C. Ropers, and S. Ashihara, "Optical field emission from resonant gold nanorods driven by femtosecond mid-infrared pulses," *AIP Adv.* **5**(7), 077138 (2015).
24. F. Kusa, I. Morichika, A. Takegami, and S. Ashihara, "Enhanced ultrafast infrared spectroscopy using coupled nanoantenna arrays," *Opt. Express* **25**(11), 12896–12907 (2017).
25. I. Morichika, F. Kusa, A. Takegami, A. Sakurai, and S. Ashihara, "Antenna-Enhanced Nonlinear Infrared Spectroscopy in Reflection Geometry," *J. Phys. Chem. C* **121**(21), 11643–11649 (2017).
26. S. Han, H. Kim, Y. W. Kim, Y. J. Kim, S. Kim, I. Y. Park, and S. W. Kim, "High-harmonic generation by field enhanced femtosecond pulses in metal-sapphire nanostructure," *Nat. Commun.* **7**, 13105 (2016).
27. M. Sivis, M. Taucher, G. Vampa, K. Johnston, A. Staudte, A. Y. Naumov, D. M. Villeneuve, C. Ropers, and P. B. Corkum, "Tailored semiconductors for high-harmonic optoelectronics," *Science* **357**(6348), 303–306 (2017).
28. G. Vampa, B. G. Ghamsari, S. S. Mousavi, T. J. Hammond, A. Olivieri, E. Lisicka-Skrek, A. Y. Naumov, D. M. Villeneuve, A. Staudte, P. Berini, and P. B. Corkum, "Plasmon-enhanced high-harmonic generation from silicon," *Nat. Phys.* **13**(7), 659–662 (2017).

29. A. E. Abbass, H. C. Swart, and R. E. Kroon, "Non-plasmonic enhancement of the near band edge luminescence from ZnO using Ag nanoparticles," *J. Lumin.* **182**, 263–267 (2017).
30. L. J. Brillson and Y. Lu, "ZnO Schottky barriers and Ohmic contacts," *J. Appl. Phys.* **109**(12), 121301 (2011).
31. S. Bayan and D. Mohanta, "Significant Fowler–Nordheim tunneling across ZnO – Nanorod based nanojunctions for nanoelectronic device applications," *Curr. Appl. Phys.* **13**(4), 705–709 (2013).
32. H. Hirori, K. Shinokita, M. Shirai, S. Tani, Y. Kadoya, and K. Tanaka, "Extraordinary carrier multiplication gated by a picosecond electric field pulse," *Nat. Commun.* **2**(1), 594 (2011).
33. B. K. Canfield, H. Husu, J. Laukkonen, B. Bai, M. Kuittinen, J. Turunen, and M. Kauranen, "Local Field Asymmetry Drives Second-Harmonic Generation in Noncentrosymmetric Nanodimers," *Nano Lett.* **7**(5), 1251–1255 (2007).
34. B. Metzger, M. Hentschel, T. Schumacher, M. Lippitz, X. Ye, C. B. Murray, B. Knabe, K. Buse, and H. Giessen, "Doubling the Efficiency of Third Harmonic Generation by Positioning ITO Nanocrystals into the Hot-Spot of Plasmonic Gap-Antennas," *Nano Lett.* **14**(5), 2867–2872 (2014).
35. T. Shibanuma, G. Grinblat, P. Albella, and S. A. Maier, "Efficient Third Harmonic Generation from Metal-Dielectric Hybrid Nanoantennas," *Nano Lett.* **17**(4), 2647–2651 (2017).
36. H. Yoshikawa and S. Adachi, "Optical Constants of ZnO," *Jpn. J. Appl. Phys.* **36**(10), 6237–6243 (1997).